Estuarine Frontogenesis

W. R. GEYER AND D. K. RALSTON

Department of Applied Ocean Physics and Engineering, Woods Hole Oceanographic Institution, Woods Hole, Massachusetts

ABSTRACT

Model studies and observations in the Hudson River estuary indicate that frontogenesis occurs as a result of topographic forcing. Bottom fronts form just downstream of lateral constrictions, where the width of the estuary increases in the down-estuary (i.e., seaward) direction. The front forms during the last several hours of the ebb, when the combination of adverse pressure gradient in the expansion and baroclinicity cause a stagnation of near-bottom velocity. Frontogenesis is observed in two dynamical regimes: one in which the front develops at a transition from subcritical to supercritical flow and the other in which the flow is everywhere supercritical. The supercritical front formation appears to be associated with lateral flow separation. Both types of fronts are three-dimensional, with strong lateral gradients along the flanks of the channel. During spring tide conditions, the fronts dissipate during the flood, whereas during neap tides the fronts are advected landward during the flood. The zone of enhanced density gradient initiates frontogenesis at multiple constrictions along the estuary as it propagates landward more than 60 km during several days of neap tides. Frontogenesis and frontal propagation may thus be essential elements of the spring-to-neap transition to stratified conditions in partially mixed estuaries.

1. Introduction

Estuaries exhibit the strongest density fronts of any marine environment because of the horizontal buoyancy fluxes from freshwater outflows augmented by tidal processes (Largier 1992; O'Donnell 1993). Surface fronts in estuaries, notable for distinct foam lines, slicks, and color changes, have received considerable attention in the dynamics literature. Examples include tidal intrusion fronts (Simpson and Nunes 1981), axial convergence fronts (Nunes and Simpson 1985), and plume fronts (Garvine 1974; O'Donnell et al. 1998; Kilcher and Nash 2010). Less conspicuous at the surface, but of particular dynamical importance, are salt wedge fronts (Keulegan 1966; Jirka and Arita 1987; Geyer and Farmer 1989), which occur where a strong salinity gradient intersects the bottom of the estuary. Bottom fronts mark the landward limit of the salinity intrusion in a salt wedge estuary (Ralston et al. 2010), but similar frontal structures occur in partially mixed estuaries (Geyer et al. 1998) and fjords (Lavelle et al. 1991). Whereas the steady-state dynamics of these

fronts have been characterized (e.g., Keulegan 1966; Armi and Farmer 1986, Jirka and Arita 1987), their genesis has received scant attention, with the notable exception of the laboratory studies of Simpson and Linden (1989).

Simpson and Linden (1989) were the first to address estuarine frontogenesis, wherein they demonstrated via laboratory experiments that a local enhancement of the horizontal salinity gradient induces a flow convergence via the baroclinic pressure gradient, which amplifies the salinity gradient and produces a front. The front then propagates into unstratified water as a lock exchange (essentially a local manifestation of the estuarine circulation), which restratifies the water column by the straining of the along-estuary density gradient by the baroclinically induced shear. Simpson and Linden (1989) showed that frontogenesis requires a convergence in the advection of the along-estuary density gradient, that is,

$$\frac{\partial}{\partial x}\left(u\left|\frac{\partial \rho}{\partial x}\right|\right) < 0, \qquad (1)$$

where u is the along-estuary velocity (typically dominated by the tidal flow, but also influenced by baroclinicity), and $\partial \rho/\partial x$ is the along-estuary density gradient. Frontogenesis can occur for either sign of $\partial \rho/\partial x$—if the flow is in the direction of increasing density

Corresponding author address: W. R. Geyer, Department of Applied Ocean Physics and Engineering, Mail Stop 11, Woods Hole Oceanographic Institution, Woods Hole, MA 02543.
E-mail: rgeyer@whoi.edu

(i.e., ebb), a bottom front forms, and for the reverse direction, a surface front forms. In their experiments, Simpson and Linden satisfied the condition of Eq. (1) by imposing a change in the strength of the along-estuary density gradient, and they note in their discussion that "frontogenesis, therefore, relies on a non-uniformity in the horizontal density variation" (Simpson and Linden 1989, p. 15). In other words, formation of a front requires that there already be a local maximum in the density gradient.

However, another possibility exists, which may be more relevant to real estuaries. Even with a uniform density gradient, Eq. (1) can be satisfied with a velocity convergence. This condition was not observed in the uniform channel of the Simpson and Linden experiments. In contrast, real estuaries have ample geometric variations to provide horizontal convergences and means for generating fronts autonomously. The frontal conditions described by Armi and Farmer (1986) are examples of fronts associated with topography, with application to estuaries described by Largier (1992). However, the theory of Armi and Farmer does not investigate the creation of a front from initially nonfrontal conditions.

This study examines an estuary, the Hudson, which exhibits pronounced frontogenesis, even with relatively modest cross-sectional variability. Frontal processes in the Hudson have been noted previously, particularly in context with the trapping of sediment (Geyer et al. 1998; Woodruff et al. 2001; Traykovski et al. 2004; Ralston et al. 2012). Ralston et al. (2008) noted that the horizontal salinity gradient in the Hudson varies through the spring–neap cycle, with the maximum salinity gradient propagating landward from near the mouth starting at the transition from spring to neap tides. The salinity front propagation was strongly associated with the spring-to-neap transition in stratification, suggesting a linkage between frontogenesis and the spring–neap transition in estuarine stratification (Haas 1977).

In this paper, we use a numerical model to examine the mechanism of frontogenesis in the Hudson estuary and to demonstrate the fundamental role that frontogenesis plays on the spring–neap variation of estuarine salinity structure and stratification. Observations confirm the numerical results with respect to the structure and propagation of the fronts.

2. Methods

A number of previously published studies document the presence of fronts in the Hudson estuary and the associated variations in salinity structure through the spring–neap cycle. These frontal observations (Bowen and Geyer 2003; Ralston et al. 2008) are reviewed in
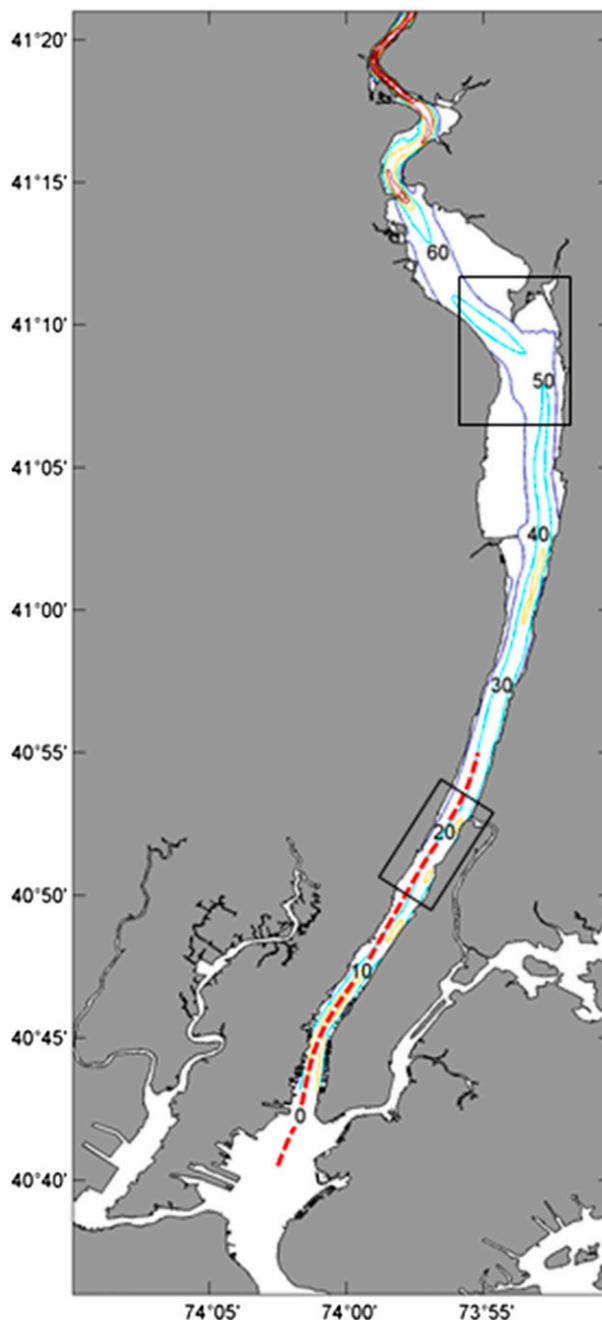

FIG. 1. Map of the Hudson estuary, with kilometers indicated. Depth contours for the river are shown in increments of 5 m. The rectangles indicate areas in which detailed model results are presented. The red dashed line indicates the location of the transect shown in Fig. 3.

context with the mechanisms of frontogenesis and provide motivation for the modeling work. Bowen and Geyer (2003) observed the formation of a front near the mouth of the estuary during a high flow event. Ralston et al. (2008) obtained time series salinity data at seven locations along the estuary (Fig. 1) over a 3-month
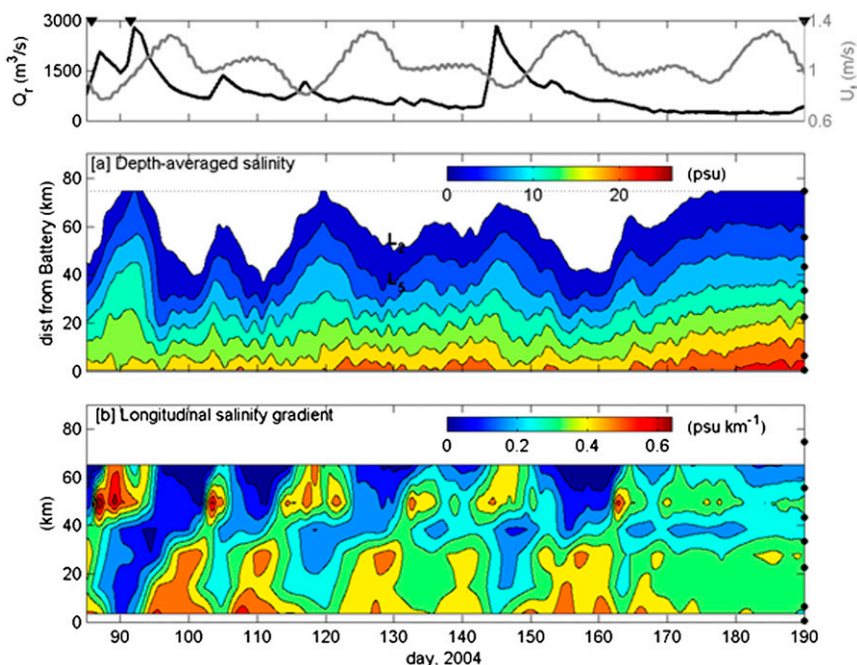
FIG. 2. Time series observations of the (a) along-estuary salinity distribution and (b) along-estuary near-bottom salinity gradient in the Hudson estuary, showing its dependence on (top panel) river discharge Q_f and tidal velocity U_T, from Ralston et al. (2008). The location and intensity of the maximum salinity gradient has a distinct dependence on the spring–neap variations of tidal amplitude, and the zone of intensified gradient propagates up estuary during neap tides. Mooring locations are shown as dots on the right axis and are indicated as circles in Fig. 1.

interval that demonstrates the time evolution of the salinity gradient because of variations in river flow and tidal amplitude.

Model simulations were performed using the Regional Ocean Modeling System (ROMS) with realistic topography of the Hudson estuary and realistic tidal forcing [as in Warner et al. (2005) and Ralston et al. (2012)], but constant river outflow of $600 \, \mathrm{m^3 \, s^{-1}}$ (close to the annual average flow of $550 \, \mathrm{m^3 \, s^{-1}}$). The spring–neap modulation of tidal amplitude was found to be an important factor influencing the frontogenesis process. River flow variations are also potentially important, but the combination of tidal variability and river flow variability would make it difficult to distinguish their separate contributions, so only tidal variability was considered in this investigation. The grid resolution in the estuary was approximately 40 m in the cross-estuary and 200 m in the along-estuary direction. This resolution was adequate to resolve the hydrostatic dynamics relevant to frontogenesis, but nonhydrostatic effects are not considered. Nonhydrostatic effects may slightly alter the criticality conditions that lead to frontogenesis, and the hydrostatic model will not represent vertical flow separation as a potential mechanism of frontogenesis. The nonhydrostatic aspects of frontogenesis would require much higher

spatial resolution and are beyond the scope of this investigation.

3. Observations

The time series observations of Ralston et al. (2008) indicate that the salinity gradient varies spatially not only because of changes in river flow but also because of the spring–neap variation in tidal amplitude (Fig. 2). The maximum salinity gradient occurs near the mouth around the time of spring tide, and the high-gradient zone propagates landward up the estuary for roughly 10 days, until the beginning of the next spring tide. The propagation speed of the front is roughly $6 \, \mathrm{km \, day^{-1}}$ (or $0.05 \, \mathrm{m \, s^{-1}}$), but it is not uniform along the estuary. Moreover, the gradient is intensified at certain locations, most notably around 50 km, although it is coarsely resolved by the roughly 10-km spacing of the moored salinity array.

A set of along-estuary salinity transects obtained during a study of the Hudson estuary described by Bowen and Geyer (2003) provides adequate spatial and temporal resolution to document an example of estuarine frontogenesis. After several months of low flow conditions, a rainfall event caused the river flow to
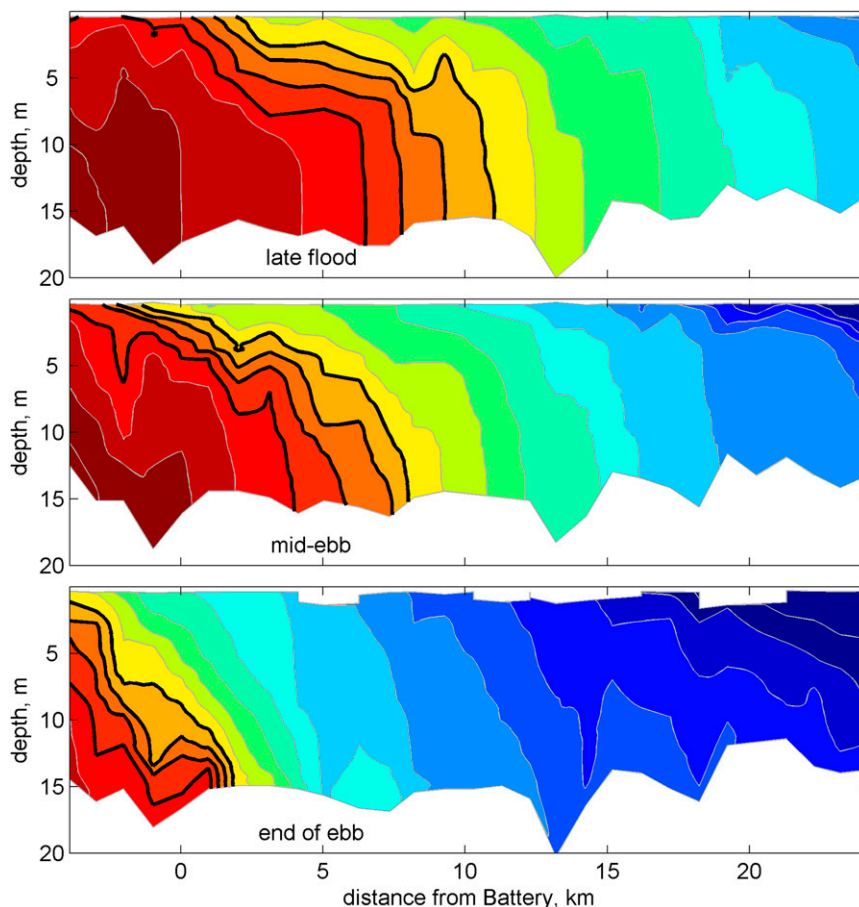
FIG. 3. Salinity cross sections at 2.5-h intervals illustrating frontogenesis in the Hudson estuary during the ebb tide, following an increase in river discharge from 200 to $1500 \, m^3 \, s^{-1}$ [observations from 22 Oct 1995, described by Bowen and Geyer (2003)]. Salinity contour interval is 1 psu, and the bold contours are the 21–24-psu contours in each figure.

increase from 200 to $1500 \, m^3 \, s^{-1}$. The greater outflow caused an intensification of the salinity gradient near the mouth (Fig. 3), starting with a distinct tilt of the pycnocline near the surface during late flood and early ebb, and culminating in a strong bottom front at kilometer 2 at the end of ebb (Fig. 3, bottom panel). Estimation of the baroclinic pressure gradient based on the salinity distribution at the end of ebb indicates a local maximum in adverse pressure gradient (i.e., decelerating the near-bottom ebb flow) with a magnitude reaching $0.18 \, Pa \, m^{-1}$; this is comparable to the maximum seaward barotropic gradient of $0.2 \, Pa \, m^{-1}$ based on scaling the tidal momentum equation. The formation of the front at this location is hypothesized to be the result of the expansion in width at the mouth of the estuary, which produces a hydraulic response of the pycnocline, generating the adverse pressure gradient and leading to frontogenesis, as will be described in detail with the model results.

4. Model results

The observations suggest that frontal processes are affected by both spring–neap variations in tidal amplitude and changes in river flow. The simulations presented here only considered the tidal contributions to the time dependence of the forcing, in order to focus on the frontogenesis mechanism in context with semidiurnal and fortnightly tidal variations. The ability of the model to simulate the full suite of forcing variables has been well demonstrated by Ralston et al. (2012, 2013).

The simulation (Fig. 4) reproduces a similar pattern of spring–neap variation in the along-estuary salinity structure as the time series observations (cf. Fig. 2), although with considerably greater along-estuary resolution. Both observations and model indicate propagation of the front from 30 to 60 km in roughly 5 days during the transition from spring to neap tides. The length of the salt intrusion is shortest, several days after spring tides,
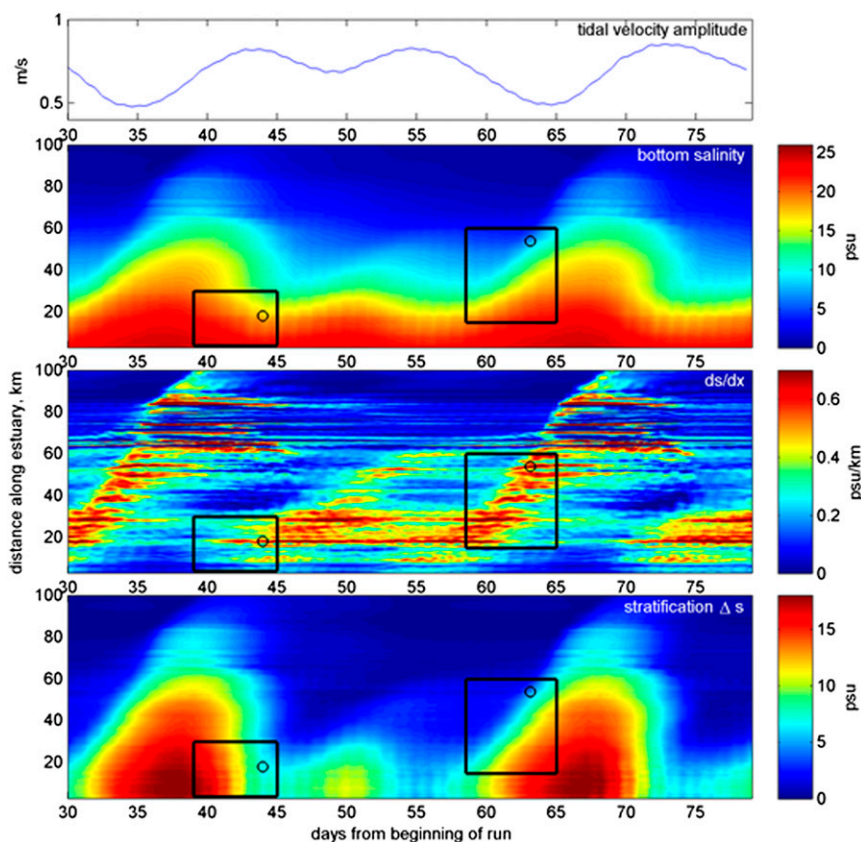
FIG. 4. Model-generated along-estuary salinity distribution as forced by spring–neap tidal variation, with constant river discharge of $600 \, \mathrm{m^3 \, s^{-1}}$. (first panel) A representative amplitude of the tidal velocity; (second panel) salinity as a function of time and distance along the estuary (with tidal variations removed with a 35-h filter); (third panel) the along-estuary salinity gradient, $\partial s/\partial x$ (psu km^{-1}; note the color map does not resolve the full range of the data); and (fourth panel) surface-to-bottom salinity difference. The tidal variations have been filtered out of all of the variables in this figure. The horizontal "stripes" in $\partial s/\partial x$ indicate that stronger gradients persist in certain locations. The multiple diagonal trends of $\partial s/\partial x$ indicate up-estuary propagation of the frontal zone. The boxes and dots indicate locations of more detailed views of the same data shown in subsequent figures.

and it reaches its maximum landward extent several days after the neap. The salinity gradient $-\partial s/\partial x$ correspondingly is greatest near the mouth following the spring tide, and the position of the enhanced salinity gradient propagates up the estuary from near the mouth to at least 100 km. The extent of propagation of the salinity gradient depends on the amplitude of the neap tide, with the greatest landward penetration of the frontal zone during weak (apogean) neaps. Distinct "hotspots" of the salinity gradient occur at specific locations along the estuary, as indicated by horizontal bands of intensified $\partial s/\partial x$. Once a strong gradient is established at each of these hotspots, it tends to persist for 5 or more days, but the initiation of the intensified gradient corresponds with the propagation of the main estuarine salinity gradient signal past that location.

The stratification shows a distinct spring–neap cycle (bottom panel of Fig. 4). Maximum stratification occurs during the weak neaps in the lower estuary, and the region of enhanced stratification propagates up estuary with a similar timing and along-estuary distribution as the bottom salinity and $\partial s/\partial x$. Stratification decreases rapidly and almost simultaneously along the estuary during spring tides.

Two time periods were selected to investigate the time progression of the salinity gradient. The period from days 39 to 45 is a transition from neap to spring tides that illustrates the initiation of the front near the mouth (Figs. 4 and 5). Significant gradients first appear around kilometer 18 at the end of day 39, and the gradients continue to increase at this location for the next 5 days. The maximum gradients occur at the end of the ebb,
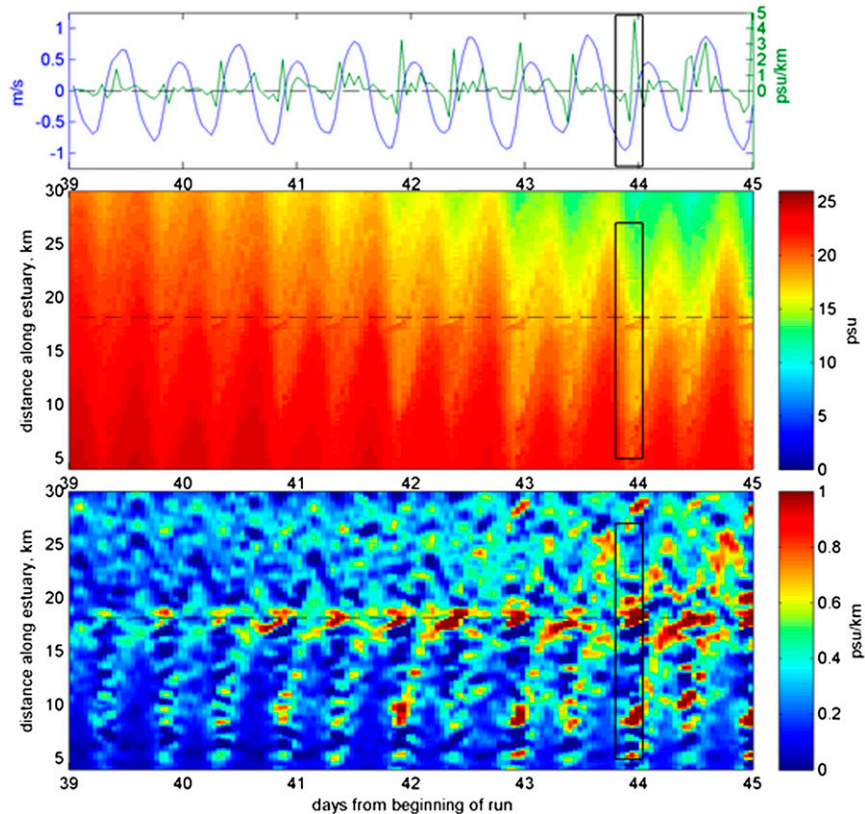
FIG. 5. Detail of the salinity gradient during days 39–45 (left box in Fig. 4), showing tidal variations of velocity, salinity, and $\partial s/\partial x$ during spring tide conditions, when the salinity front becomes reestablished in the lower estuary. (top) The blue curve is vertically averaged, along-estuary velocity, and the green curve is $-\partial s/\partial x$ (psu km^{-1}) at km 16.3; (middle) salinity (psu) and (bottom) $\partial s/\partial x$ (psu km^{-1}) along the thalweg. Note that the maximum salinity gradient occurs at the end of the ebb tide.

reaching 5 psu km^{-1} at 18 km (Fig. 5, upper panel). During this time interval, the high-gradient zone propagates landward several kilometers during the ensuing flood tides, but the along-estuary coherence of the gradient zone is much smaller than the tidal excursion scale of 8–10 km.

Along-estuary sections of salinity and velocity provide a detailed look at the process of frontogenesis in the lower estuary (Fig. 6). The top panels indicate the along-estuary distribution of near-bottom $\partial s/\partial x$ (note that the sign is changed for clarity of presentation) and near-bottom velocity at hourly intervals from midebb to early flood. The other panels show the vertical distributions of salinity and velocity at each time interval. At around maximum ebb, the salinity gradient is relatively uniform through this reach of the estuary. As the ebb progresses, the pycnocline steepens around 17 km, and the near-bottom velocity decreases below the tilted pycnocline. The front steepens as the ebb continues (third and fourth panel), and the near-bottom flow decreases and

actually reverses in the zone from 15 to 17 km, while the near-surface currents still exceed 1.2 m s^{-1}. The reversal of near-bottom velocity at that location results in a strong convergence of near-bottom velocity, which leads to a convergence of salinity contours and the generation of a bottom salinity front. In the final panel, the front begins to propagate landward as the near-bottom current becomes landward-directed throughout the reach.

The steepening of the pycnocline and the subsequent intensification of the near-bottom salinity gradient contribute to a local intensification of the baroclinic pressure gradient within the frontal zone, as shown in Fig. 7 for the period of maximum frontogenesis. Upstream of the developing front (kilometers 17.5–19), the baroclinic gradient (thin lines in Fig. 7) is weak, but it reaches a local extremum of -0.28 Pa m^{-1} (i.e., Nt m^{-3}) on the downstream side of the developing front. Note that this is similar in magnitude to the baroclinic gradient estimated in the field data (Fig. 3). The baroclinic
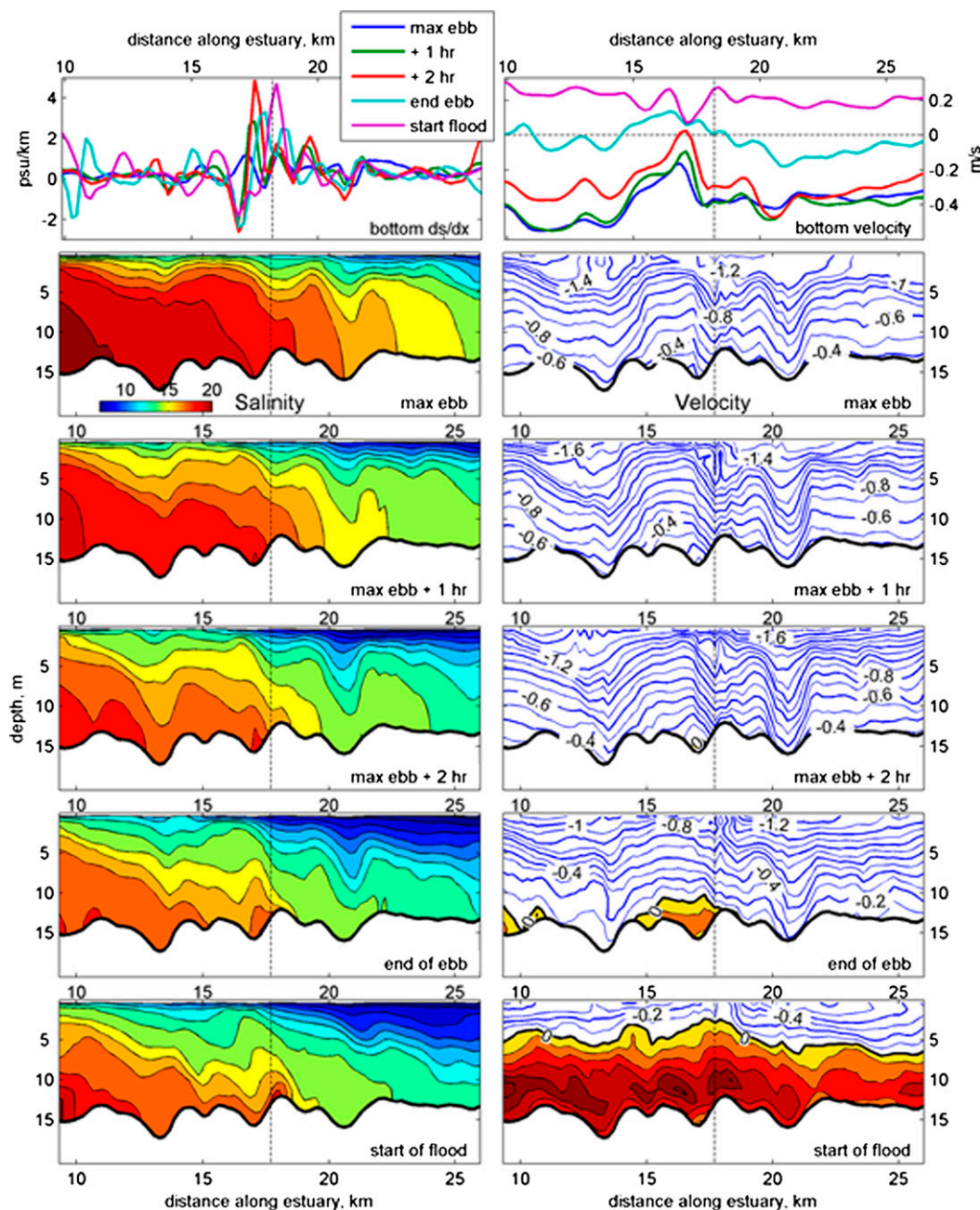
FIG. 6. Conditions at the lower-estuary frontal zone at various times during the ebb on day 43.9. (top left) Bottom salinity gradient $-\partial s/\partial x$; (top right) near-bottom velocity; (bottom left) salinity contours; and (bottom right) along-estuary velocity contours. Dashed line corresponds to km 18, where the maximum gradient occurs. Flooding currents are indicated with color contours in the right panels.

gradient is strong enough that it reverses the total pressure gradient at the bottom (thick lines in Fig. 7), resulting in a sharp reversal in the pressure gradient across the frontal zone. This change in sign of the near-bottom pressure gradient drives the strong convergence of near-bottom velocity across the frontal zone (top-right panel of Fig. 6).

Note that the change from a favoring to adverse pressure gradient occurs at other locations in the lower estuary (e.g., 11 and 13 km), and the upper-left panel of Fig. 6 indicates evidence of frontogenesis just seaward of these locations at the start of the flood. The variability of topography thus provides a variety of sites for frontogenesis, some stronger than others, depending
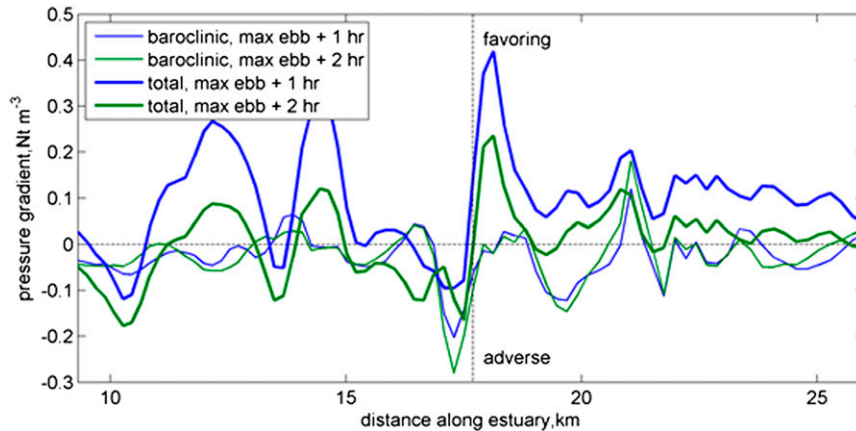
FIG. 7. Baroclinic and total pressure gradient at the bottom grid cell along the thalweg during the ebb when frontogenesis at kilometer 17.7 is maximal. Favoring (accelerating) pressure gradient is positive, and adverse (decelerating) is negative. The baroclinic pressure gradient in the developing front is strong enough to produce an abrupt reversal of the near-bottom pressure gradient at the location of frontogenesis, leading to intense convergence of near-bottom velocity.

on the geometry as well as the preexisting salinity structure.

The period from days 58 to 65 is a transition from spring to neap (cf. Fig. 4) that illustrates the landward propagation of the front, shown in detail in Fig. 8. During this period, the main salinity gradient zone appears as a landward-propagating group of multiples fronts, in contrast with the more stationary frontal conditions observed near the mouth during spring tides (Fig. 5). The gradients are intensified at specific along-estuary positions, but the fronts remain more coherent through the tidal cycle than during spring tides, allowing the frontal signal to propagate landward in the estuary. Individual frontal filaments can retain their coherence for up to several days, but in other instances the front dissipates and reforms each tidal cycle. The excursions of the fronts in one tidal cycle are slightly less than 10 km and are comparable to the tidal excursion calculated from near-bottom velocities.

Within the general landward progression of the salinity gradient, frontogenesis is observed at a number of locations, almost always during the second half of the ebb tide. One such location is near kilometer 54, at which frontogenesis becomes evident around day 62 and reaches its maximum expression on day 63 (Fig. 8, top panel). A sequence of hourly salinity and velocity sections at this location (Fig. 9) shows the strong amplification of the salinity gradient from midebb to the start of the flood. As with the lower-estuary front, the salinity gradient in this zone amplifies during the late ebb as the isopycnals steepen, which causes the near-bottom velocity to weaken and reverse. The near-bottom velocity reversal results in strong convergence and rapid frontogenesis. Note that the

near-bottom velocity reversal occurs within 1 h of maximum ebb at this location, providing a 4-h period of stationary conditions for the front to develop. This contrasts the lower-estuary front, which has less than 2 h of stationary conditions and has much more variability of frontal position during its formation.

The intensifying salinity gradient within the frontal zone contributes to a strong intensification of the baroclinic pressure gradient (Fig. 10), with a similar magnitude as the lower-estuary frontal zone. Similar to the lower-estuary case, the total near-bottom pressure gradient reverses across the frontal zone, driving the near-bottom velocity convergence (Fig. 9, top-right panel).

Plan views and cross sections of the salinity structure at these two frontal zones at the end of ebb (Fig. 11) indicate that these fronts are inherently three-dimensional, with marked cross-estuary structure. The front at 54 km is almost symmetrical with respect to the thalweg, with the nose of the front centered on the thalweg and flanks that extend downstream on either side, oblique but nearly parallel to the channel. The near-bottom flow is convergent along this frontal zone. Note that the geometry of this front is similar to a tidal intrusion front (Simpson and Nunes 1981), except that it is at the bottom instead of the surface. The analysis in the following section confirms that the dynamics are also similar in that the front is in essence an arrested gravity current (Britter and Simpson 1981), with a propagation speed that is matched by the ebb velocity at the throat of the constriction.

The lower-estuary front at 18 km has a different geometry (Fig. 11). It is asymmetric with respect to the
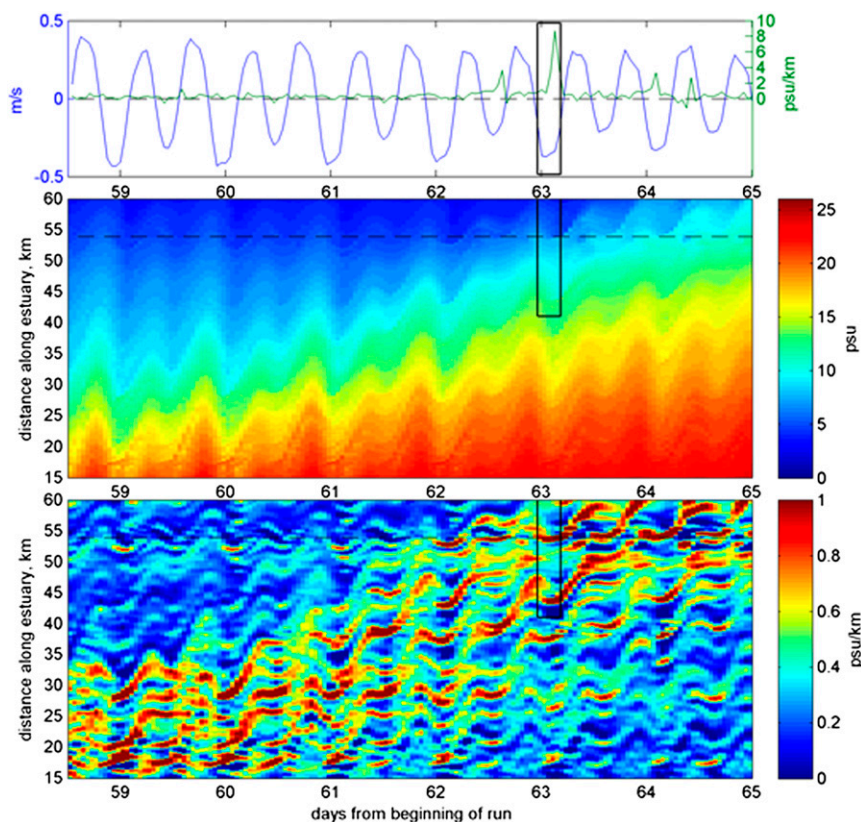
FIG. 8. Detail of the salinity gradient during days 59–65 (right box in Fig. 4), showing tidal variations of velocity, salinity and $\partial s/\partial x$ during neap–tide conditions, when the frontal zone is propagating up-estuary. (top) The blue curve is vertically averaged, along-estuary velocity, and the green curve is $-\partial s/\partial x$ (psu km^{-1}) at kilometer 52; (middle) salinity and (bottom) $\partial s/\partial x$ (psu km^{-1}). At kilometer 52, the maximum salinity gradient occurs at the end of the ebb tide, but the bottom front maintains its integrity as it propagates landward through the flood. Note that there are multiple fronts during this time interval.

channel, and the frontal zone extends from the shore at the tip of a headland, indicating lateral flow separation. This frontal zone was described by Chant and Wilson (1997) as a headland eddy resulting from lateral flow separation. The front extends across the estuary at a highly oblique angle to the channel. The near-bottom flow is convergent but is nearly parallel to the front over most of its extent. The analysis in the following section indicates that some aspects of the frontogenesis are similar for these two frontal zones, but the dynamics have distinct differences because of the internal hydraulics of the two regimes.

5. Analysis

a. Frontogenesis

The rate of frontogenesis in the along-estuary (x) direction can be expressed by taking the horizontal derivative of the salinity tendency equation:

$$\frac{\partial}{\partial t}\frac{\partial s}{\partial x} + \mathbf{u}\cdot\nabla\frac{\partial s}{\partial x} = -\frac{\partial u}{\partial x}\frac{\partial s}{\partial x} - \frac{\partial v}{\partial x}\frac{\partial s}{\partial y} - \frac{\partial w}{\partial x}\frac{\partial s}{\partial z} - \frac{\partial}{\partial x}\frac{\partial}{\partial z}\overline{s'w'},$$

(2)

where the first term is the local tendency of the salinity gradient, the second term is the advection of the gradient, and the third term is the horizontal convergence. The fourth and fifth terms represent twisting because of the along-estuary gradients in lateral and vertical velocity, and the last term is the along-estuary gradient of vertical mixing. Any one of the terms on the right-hand side could lead to frontogenesis depending on the conditions in the estuary, and each of them plays a role in frontogenesis in the Hudson at different places and times. However, the most obvious mechanism, and the one highlighted by Simpson and Linden (1989), involves the first term on the right—the horizontal convergence of salinity gradient. During conditions in which the near-bottom flow is convergent but includes a stagnation
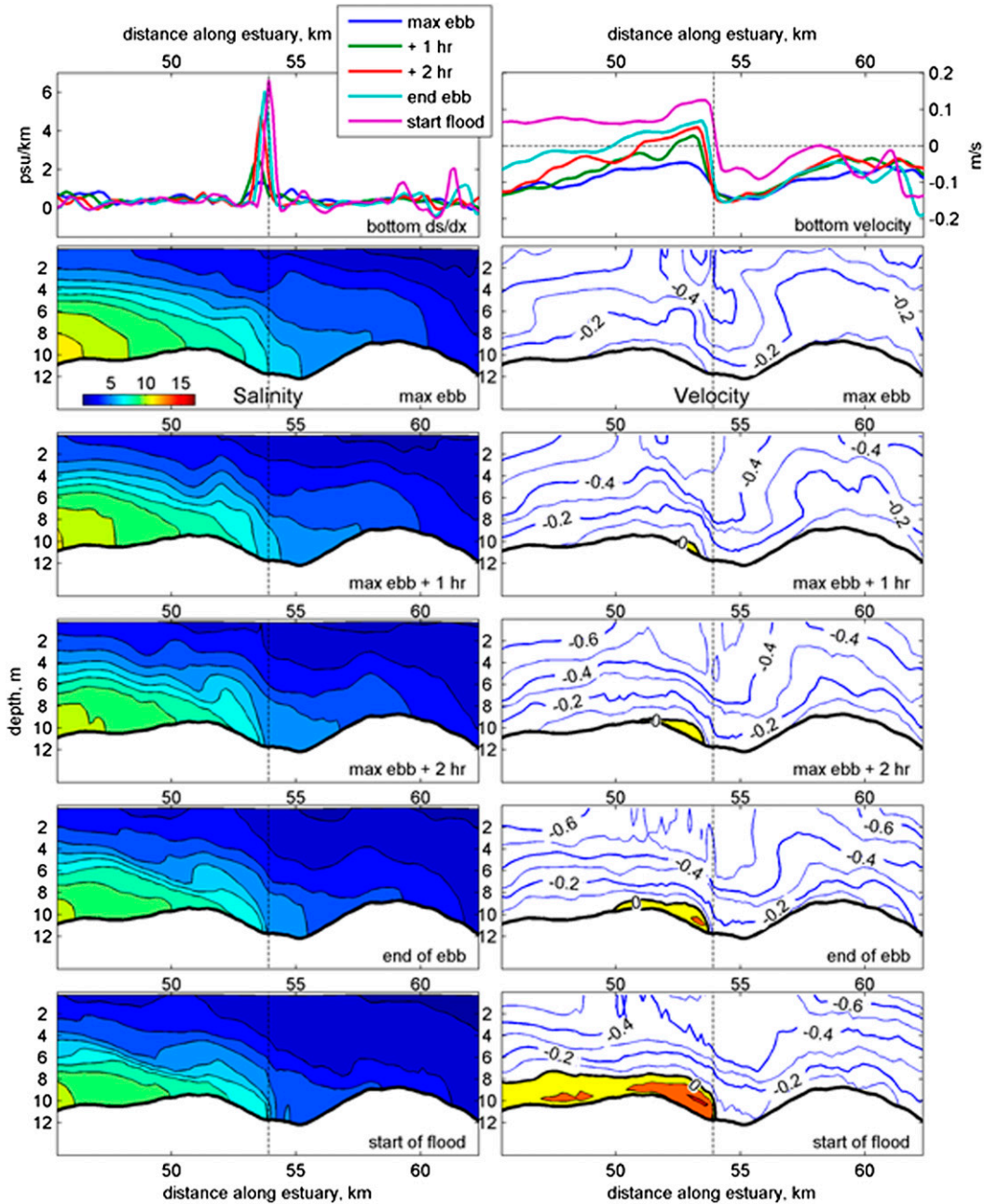
FIG. 9. Conditions at the upper-estuary frontal zone at various times during the ebb on day 63.2. (top left) Bottom salinity gradient $-\partial s/\partial x$; (top right) near-bottom velocity; (bottom left) salinity contours; and (bottom right) along-estuary velocity contours. Dashed line corresponds to kilometer 52, where the maximum gradient occurs. Flooding currents are indicated with color contours in the right panels.

point (e.g., Fig. 9, top-right panel), the advective term can be neglected at the stagnation point, leading to an approximate balance between time dependence and horizontal convergence:

$$\frac{\partial}{\partial t}\frac{\partial s}{\partial x} \cong -\frac{\partial u}{\partial x}\frac{\partial s}{\partial x}. \tag{3}$$

Under these conditions, the salinity gradient increases exponentially, with an *e*-folding time scale of $\partial u/\partial x^{-1}$. The amplitude of $\partial u/\partial x$ at the lower- and upper-estuary frontal zones are $1 \times 10^{-3}\,\mathrm{s}^{-1}$ and $0.5 \times 10^{-3}\,\mathrm{s}^{-1}$, respectively, with corresponding *e*-folding scales of 15 and 30 min. These convergence rates would result in a 7–50-fold amplification of the gradient in 1 h. The amplification
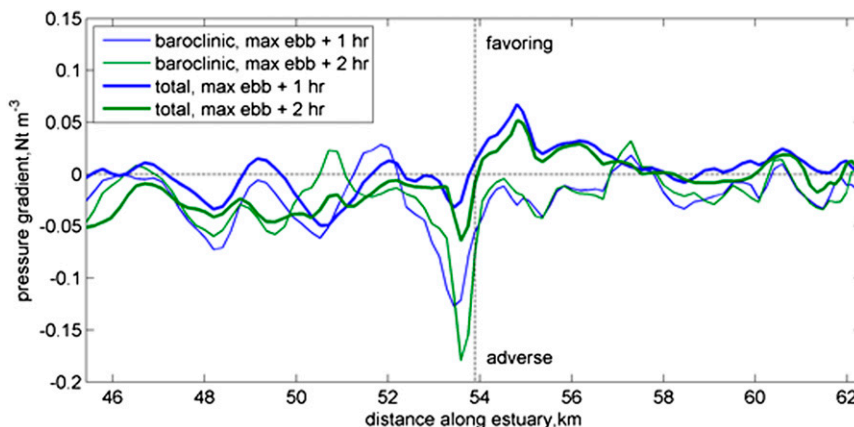
FIG. 10. Baroclinic and total pressure gradient at the bottom grid cell along the thalweg during the ebb when frontogenesis at kilometer 54 is maximal. Just as at the lower-estuary frontal zone, the baroclinic pressure gradient reverses at the location of frontogenesis, leading to intense convergence of near-bottom velocity.

of the gradient at the northern site was approximately consistent with Eq. (3), whereas the rate was approximately half of that predicted by Eq. (3) at the southern site. The relatively slower growth at the southern site is explained by other terms from Eq. (2), particularly the advective term because of the finite near-bottom velocities during maximum convergence. The convergence rate estimates confirm that horizontal convergence can explain the rapid increase in salinity gradient at both sites. It remains to be demonstrated what causes the intense, localized convergence.

A total of nine prominent frontal zones were identified in the estuary based on the strength of the near-bottom salinity gradient at some point in the spring–neap cycle. Of these, seven showed maximum frontogenesis during late ebb, consistent with the two frontal zones that were described in detail. The other two occurred in the geometrically complex region between kilometers 62 and 68, and the frontogenesis mechanism for those locations could not be discerned in this analysis. For all but one of the frontal locations, the consistent topographic feature among them was an along-estuary change in width (Fig. 12). All of these fronts occur in zones with lateral expansions extending several channel widths in the down-estuary direction. In some cases, the change in width is slight (e.g., kilometer 28), and in others it is large in amplitude relative to the width (e.g., kilometer 55).

Another factor influencing frontogenesis may be the spacing of the expansions. The modest expansion at kilometer 28 is one tidal excursion north of the more prominent expansion at kilometer 17, and the landward advection of the frontal zone appears to promote the development of a frontal zone upstream (cf. Fig. 8). In

fact, the frontogenesis mechanism described by Simpson and Linden (1989) is based on the preexistence of a local maximum in $-\partial s/\partial x$, which would provide an initial baroclinic contribution to velocity convergence.

The influence of a change in width on the dynamics of a stratified flow can be examined with two-layer, inviscid hydraulic theory. For a flow in which the velocity in the upper layer u_1 is much greater than in the lower layer u_2, the response of the interface elevation h_i to a change in width W can be expressed as

$$\frac{\partial h_i}{\partial x} = \frac{\mathrm{Fr}_1^2}{(G^2 - 1)} \frac{h_1}{W} \frac{\partial W}{\partial x}, \qquad (4)$$

where Fr_1 and Fr_2 are layer Froude numbers, and G is the composite Froude number

$$\mathrm{Fr}_1^2 = \frac{u_1^2}{g'h_1}, \quad \mathrm{Fr}_2^2 = \frac{u_2^2}{g'h_2} \quad \text{and} \quad G^2 = \mathrm{Fr}_1^2 + \mathrm{Fr}_2^2. \qquad (5)$$

The quantity h_1 is the thickness of the upper layer, and $g' = \Delta\rho/\overline{\rho}g$ is the reduced gravity based on the density difference between the layers (Farmer and Freeland 1983; Armi and Farmer 1986; Geyer and Ralston 2011). For supercritical Froude numbers, that is, $G > 1$, the interface rises as the width increases, as with a liftoff front at the mouth of an estuary (MacDonald and Geyer 2004; Armi and Farmer 1986). In context with frontogenesis, we consider the supercritical response of the interface before the front has formed, for example, panels 1–3 in Figs. 6 and 9.

Although the water column is continuously stratified, we estimate the layer Froude number based on assigning
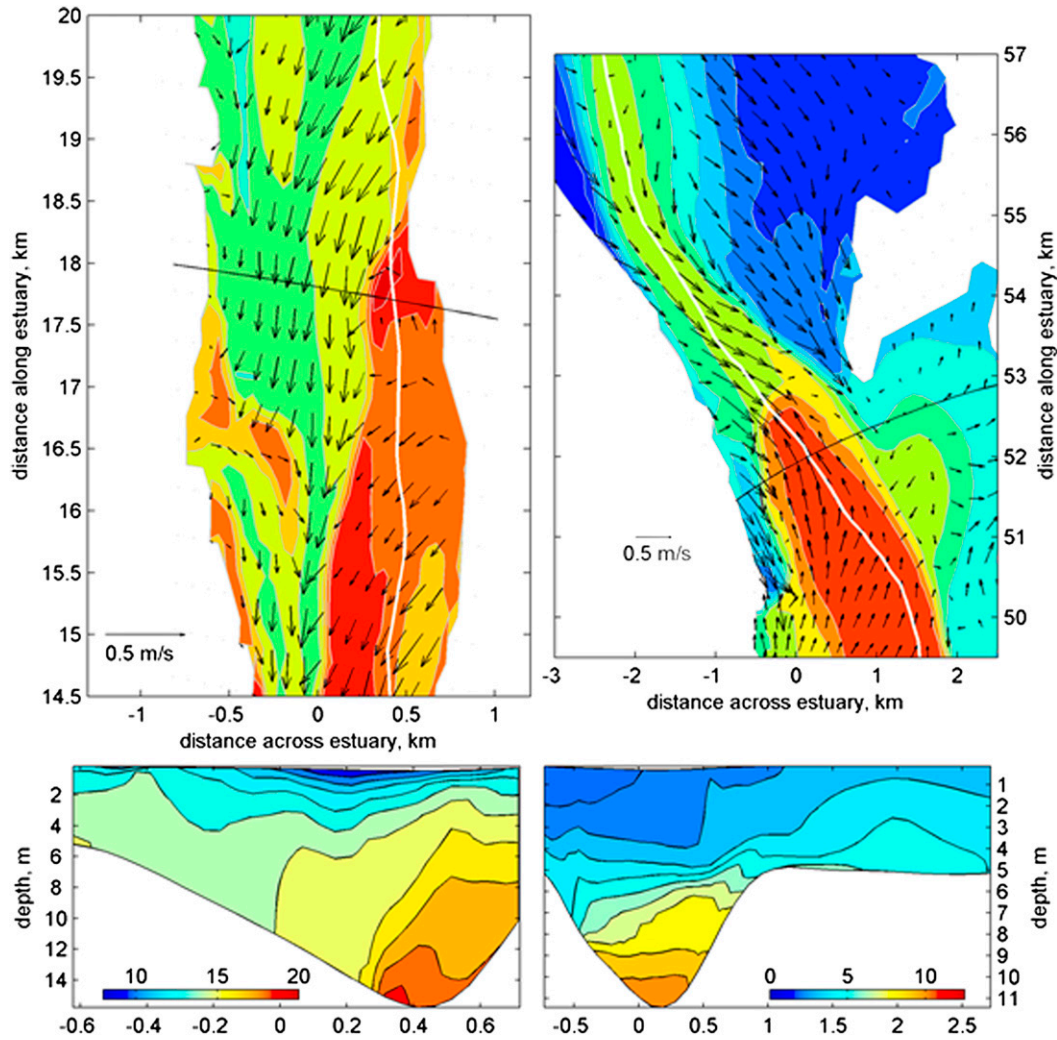
FIG. 11. Plan view of (top) bottom salinity and (bottom) transverse cross sections of salinity at frontal zones at 18 and 54 km at the end of ebb (corresponding to the second to bottom panel of Figs. 7 and 9). The arrows indicate near-bottom velocity. The thalweg is indicated as a white line. Note that the front has marked transverse structure, with comparable gradients in the cross-estuary as along-estuary direction.

a particular salinity level s_{mid} as the interface height and averaging the velocity and salinity above and below that level to obtain the layer values. The value of s_{mid} was determined at each location as the midpoint between its minimum and maximum value. Only the along-channel component of velocity was considered for the calculation.

The distributions of composite Froude number G are shown in Fig. 13 for the late-ebb conditions in the two frontal zones. The southern frontal zone is strongly supercritical throughout the zone of frontogenesis through the late ebb (left panels). The sharp rise in the pycnocline near kilometer 17 is consistent with the supercritical conditions in the expansion during the late-ebb flow [Eq. (4)]. The strong tilt of the pycnocline supplies the

baroclinicity that causes the convergence of along-estuary flow and leads to frontogenesis.

The persistently supercritical conditions would lead to rapid retreat of the front if it were oriented normal to the flow, but the front remains stationary because of its oblique orientation to the flow (Fig. 11), consistent with the Froude angle concept discussed by MacDonald and Geyer (2005). The angle φ of the front to the flow is approximately 25° during late ebb (Fig. 11, left panel), and the component of the Froude number normal to the flow is $G\sin\varphi$. At the end of ebb, $G = 2.4$, so the front-normal Froude number is close to 1, consistent with stationary frontal conditions.

The composite Froude number at the northern frontal zone is also supercritical during late ebb (Fig. 13, right
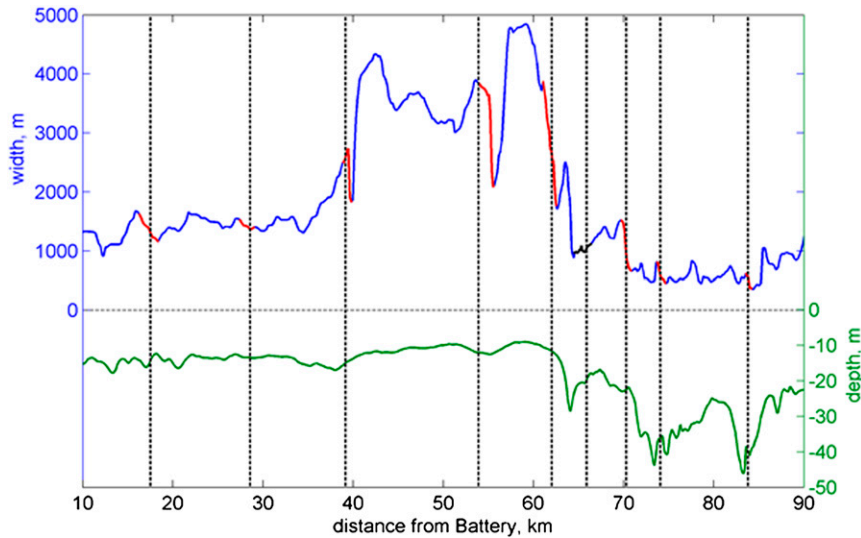
FIG. 12. Width and depth along the estuary, showing the locations of prominent fronts that form during the late ebb. The red highlight indicates the expansion of width in the downstream direction that corresponds with each frontal zone. Only the front at 66 km does not occur at an expansion.

panels), resulting in an upward tilt of the pycnocline in the expansion between 52 and 54 km. At this frontal zone the flow is close to critical for several hours during the late ebb, and the nose of the front is oriented normal to the flow (Fig. 11, upper-right panel). This regime is essentially an arrested gravity current (Britter and Simpson 1981; Armi and Farmer 1986), with the position of the front dictated by the velocity at the throat of the constriction (Fig. 11).

Calculation of the Froude numbers during the ebb at the other frontal zones suggests that all have supercritical conditions during maximum ebb in the expansion zones, consistent with the hydraulic mechanism of frontogenesis. The frontal zone at 29 km is strongly supercritical, like the lower-estuary front, but the rest of the frontal zones have nearly critical conditions during late ebb, consistent with the arrested gravity current regime as at the northern frontal zone.
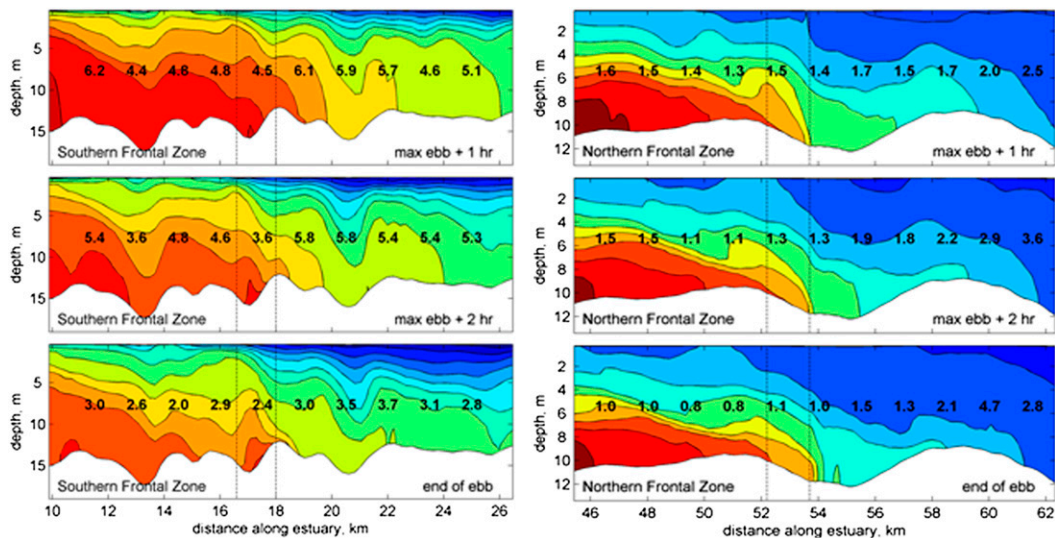

FIG. 13. Composite Froude number G during the late ebb superimposed on salinity contours at the (left) southern frontal zone and (right) northern frontal zone. Conditions are supercritical ($G > 1$) at both frontal zones (marked by vertical dashes) during the late ebb. Note that the northern frontal zone becomes critical ($G = 1$) at the end of the ebb, whereas the southern frontal zone remains supercritical.

b. The role of lateral flow separation

The lower-estuary (17 km) frontal zone persists when the Froude number in the along-estuary direction remains above one throughout the ebb, whereas the frontal zone at the midestuary location (54 km) is established only when the along-estuary flow becomes critical (Fig. 13). The front at 17 km, as well as the one at 28 km (Fig. 4), also persists through the spring–neap cycle, whereas the other frontal zones are less apparent during spring tides. The oblique orientation of the 17- and 28-km frontal zones allows them to persist through supercritical along-channel flow conditions, and although baroclinicity plays a role in the frontal formation, the geometry of the front suggests that lateral flow separation also contributes to its development. Chant and Wilson (1997) described this frontal zone in context with lateral flow separation, but they also noted the importance of baroclinicity in the dynamics. In the model results, this frontal zone is found to be stronger during spring tides when the flows are more strongly supercritical than during neaps (Fig. 4). The response during high Froude number spring tides suggests that lateral velocity gradients associated with lateral flow separation may become more important for frontogenesis than the vertical velocity gradients due to baroclinicity. Both mechanisms occur in regions of lateral expansions, and the relative contributions of lateral separation and baroclinicity may modulate with the spring–neap tidal forcing.

c. Propagation of the front

One of the notable results of this numerical study as well as previous observations by Ralston et al. (2008) is the landward propagation of the front (Figs. 2, 4). The time variation of $\partial s/\partial x$ shown in Fig. 4 indicates that the landward propagation of the frontal region only occurs during relatively weak tidal forcing. When the tidal amplitude is less than about 0.8 m s^{-1}, the front propagates landward with an average speed of roughly 0.08 m s^{-1}. Scaling of the terms in the momentum balance near the front indicates that its propagation differs markedly from an inviscid gravity current (Benjamin 1968) due to bottom friction (Geyer and Farmer 1989; Geyer and Ralston 2011). When the local contributions to along-estuary advection are averaged over scales of the tidal excursion (10 km) in the along-estuary direction, the tidally averaged dynamical balance within the frontal zone is mainly between the baroclinic pressure gradient and stress divergence within the lower layer, consistent with the expected dynamics for the estuarine circulation (Pritchard 1956; Geyer et al. 2000). However, within the frontal zone, the inflow velocity in

the lower layer is significantly enhanced relative to its time average over the simulation—0.07–0.1 m s^{-1} compared to an average of 0.03–0.04 m s^{-1}. Thus, the propagation of the front is mainly an advective process, driven by the baroclinic pressure gradient resulting from the enhanced salinity gradient in the frontal zone.

The phasing of frontal propagation relative to the spring–neap cycle remains to be determined. The frontal zone near 17 km persists through spring tides, but landward propagation of the front only commences when the tidal amplitude is less than half of its spring tide value. This inverse dependence on tidal amplitude is because of the strong sensitivity of the stratification to vertical mixing (Fig. 4). Although the baroclinic pressure gradient itself does not depend on vertical stratification, the propagation of the salt front requires that the lower-layer moves up estuary with a compensating down-estuary flow of the upper layer. Stratification suppresses turbulence in the water column, allowing the development of a two-layer flow (MacCready and Geyer 2010, and references therein). Once the tidal mixing is weak enough (around day 60 in Fig. 4), the baroclinic forcing due to the strong salinity gradient in the frontal zone results in restratification of the water column, which allows the up-estuary propagation of the front. As the front propagates up estuary, the stratification propagates with $\partial s/\partial x$, and the process continues until vertical mixing increases with the next spring tide.

6. Summary and discussion

This numerical study demonstrates that a partially mixed estuary such as the Hudson can develop strong fronts because of the interaction of the stratified flow with topography. The study focuses on bottom salinity fronts that occur in the latter part of the ebb tide, downstream of lateral constrictions. Two different types of fronts are observed. One is analogous to the tidal intrusion front, in which an arrested front develops with a critical Froude number near the throat of the constriction. The other, which occurs during supercritical flow conditions, appears to be associated with lateral flow separation. During spring tide conditions, frontogenesis only occurs because of the latter mechanism, as the water column is weakly stratified and supercritical conditions prevail through the estuary. As the tidal amplitude weakens, the salinity gradient generated in the lower estuary starts propagating northward, spawning frontogenesis at constrictions farther landward in the estuary. A strong spring–neap variation is observed in the along-estuary distribution of salinity as a result of this cyclical process of frontogenesis and frontal propagation.

The Hudson estuary has a particularly strong spring–neap signal of stratification and vertical mixing, as shown in a number of prior studies (e.g., Geyer et al. 2000; Bowen and Geyer 2003; Ralston et al. 2008) and in these model results. This study indicates that the spring–neap variation of stratification and frontogenesis are interrelated. In particular, the restratification of the estuary following the spring tide is directly related to the frontogenesis process, via the propagation of stratification up the estuary (Fig. 4, lower panel). The propagation of stratification was also demonstrated in observations reported by Ralston et al. (2008), but the role of the spring–neap variation in tidal amplitude is clearer in the absence of variations of river discharge.

Variations in river discharge were not considered in this study, but they are indeed important in the frontogenesis process. The intermediate flow conditions of this study $(600 \, m^3 \, s^{-1})$ were chosen because of the strong spring–neap response of the system. At lower flow rates, the spring–neap variation in position of the salinity front is reduced (Fig. 2; discussed in Ralston et al. 2008). At higher flow rates, the landward advance of the front is inhibited by the strong outflow. The optimal response of the system at intermediate discharge rate appears to be related to the near-critical Froude number. Supercritical flow conditions are required during the ebb for the hydraulic response that leads to frontogenesis, but propagation of the front requires a sustained period of subcritical conditions during the ensuing flood tide. Higher river discharge leads to stronger stratification and a lower Froude number for a given tidal flow, but the frontal propagation speed on the order of $0.1 \, m \, s^{-1}$ can be arrested by net outflow of similar magnitude.

Frontogenesis in the Hudson can be compared with other systems, particularly to contrast with more weakly and more strongly stratified systems, and systems with different topographic variations. These results suggest that lateral flow separation may be a more important mechanism in the high Froude number, weakly stratified estuaries, whereas baroclinic hydraulic response should be more prominent in intermediate Froude number systems. Mechanisms of frontogenesis associated with flow curvature and abrupt bottom topography may dominate in other systems and may play important roles in the Hudson. The pursuit of these mechanisms of frontogenesis is important because the occurrence of estuarine fronts is important to the dynamics and kinematics of estuaries.

REFERENCES

Armi, L., and D. M. Farmer, 1986: Maximal two-layer exchange through a contraction with barotropic net flow. *J. Fluid Mech.,* **164,** 27–51, doi:10.1017/S0022112086002458.

Benjamin, T. B., 1968: Gravity currents and related phenomena. *J. Fluid Mech.,* **31,** 209–248, doi:10.1017/S0022112068000133.

Bowen, M. M., and W. R. Geyer, 2003: Salt transport and the time-dependent salt balance of a partially stratified estuary. *J. Geophys. Res.,* **108,** 3158, doi:10.1029/2001JC001231.

Britter, R. E., and J. E. Simpson, 1981: A note on the structure of the head of an intrusive gravity current. *J. Fluid Mech.,* **112,** 459–466, doi:10.1017/S0022112081000517.

Chant, R. J., and R. E. Wilson, 1997: Secondary circulation in a highly stratified estuary. *J. Geophys. Res.,* **102,** 23 207–23 215, doi:10.1029/97JC00685.

Farmer, D. M., and H. J. Freeland, 1983: The physical oceanography of fjords. *Prog. Oceanogr.,* **12,** 147–220, doi:10.1016/0079-6611(83)90004-6.

Garvine, R. W., 1974: Dynamics of small-scale oceanic fronts. *J. Phys. Oceanogr.,* **4,** 557–569, doi:10.1175/1520-0485(1974)004<0557:DOSSOF>2.0.CO;2.

Geyer, W. R., and D. M. Farmer, 1989: Tide-induced variation of the dynamics of a salt wedge estuary. *J. Phys. Oceanogr.,* **19,** 1060–1072, doi:10.1175/1520-0485(1989)019<1060:TIVOTD>2.0.CO;2.

——, and D. K. Ralston, 2011: The dynamics of strongly stratified estuaries. *Water and Fine Sediment Circulation,* E. Wolanski and D. McLusky, Eds., Vol. 2, *Treatise on Estuarine and Coastal Science,* Academic Press, 37–51.

——, R. P. Signell, and G. C. Kineke, 1998: Lateral trapping of sediment in a partially mixed estuary. *Physics of Estuaries and Coastal Seas,* J. Dronkers and M. B. A. M. Scheffers, Eds., CRC Press, 115–123.

——, J. H. Trowbridge, and M. Bowen, 2000: The dynamics of a partially mixed estuary. *J. Phys. Oceanogr.,* **30,** 2035–2048, doi:10.1175/1520-0485(2000)030<2035:TDOAPM>2.0.CO;2.

Haas, L. W., 1977: The effect of the spring-neap tidal cycle on the vertical salinity structure of the James, York and Rappahannock rivers, Virginia USA. *Estuarine Coastal Mar. Sci.,* **5,** 485–496, doi:10.1016/0302-3524(77)90096-2.

Jirka, G. H., and M. Arita, 1987: Density currents or density wedges: Boundary-layer influence and control methods. *J. Fluid Mech.,* **177,** 187–206, doi:10.1017/S0022112087000910.

Keulegan, G. H., 1966: The mechanism of an arrested saline wedge. *Estuary and Coastline Hydrodynamics,* A. T. Ippen, Ed., McGraw-Hill, 546–574.

Kilcher, L. F., and J. D. Nash, 2010: Structure and dynamics of the Columbia River tidal plume front. *J. Geophys. Res.,* **115,** C05S90, doi:10.1029/2009JC006066.

Largier, J. L., 1992: Tidal intrusion fronts. *Estuaries,* **15,** 26–39, doi:10.2307/1352707.

Lavelle, J. W., E. D. Cokelet, and G. A. Cannon, 1991: A model study of density intrusions into and circulation within a deep, silled estuary: Puget Sound. *J. Geophys. Res.,* **96,** 16 779–16 800, doi:10.1029/91JC01450.

MacCready, P., and W. R. Geyer, 2010: Advances in estuarine physics. *Annu. Rev. Mar. Sci.,* **2,** 35–58, doi:10.1146/annurev-marine-120308-081015.

MacDonald, D. G., and W. R. Geyer, 2004: Turbulent energy production and entrainment at a highly stratified estuarine front. *J. Geophys. Res.,* **109,** C05004, doi:10.1029/2003JC002094.

——, and ——, 2005: Hydraulic control of a highly stratified estuarine front. *J. Phys. Oceanogr.,* **35,** 374–387, doi:10.1175/JPO-2692.1.

Nunes, R. A., and J. H. Simpson, 1985: Axial convergence in a well-mixed estuary. *Estuarine Coastal Shelf Sci.,* **20,** 637–649, doi:10.1016/0272-7714(85)90112-X.

O'Donnell, J., 1993: Surface fronts in estuaries: A review. *Estuaries,* **16,** 12–39, doi:10.2307/1352761.

——, G. O. Marmorino, and C. L. Trump, 1998: Convergence and downwelling at a river plume front. *J. Phys. Oceanogr.,* **28,** 1481–1495, doi:10.1175/1520-0485(1998)028<1481:CADAAR>2.0.CO;2.

Pritchard, D. W., 1956: The dynamic structure of a coastal plain estuary. *J. Mar. Res.,* **15,** 33–42.

Ralston, D. K., W. R. Geyer, and J. A. Lerczak, 2008: Subtidal salinity and velocity in the Hudson River estuary: Observations and modeling. *J. Phys. Oceanogr.,* **38,** 753–770, doi:10.1175/2007JPO3808.1.

——, ——, and ——, 2010: Structure, variability, and salt flux in a strongly forced estuary. *J. Geophys. Res.,* **115,** C06005, doi:10.1029/2009JC005806.

——, ——, and J. C. Warner, 2012: Bathymetric controls on sediment transport in the Hudson River estuary: Lateral asymmetry

and frontal trapping. *J. Geophys. Res.,* **117,** C10013, doi:10.1029/2012JC008124.

——, J. C. Warner, W. R. Geyer, and G. R. Wall, 2013: Sediment transport due to extreme events: The Hudson River estuary after tropical storms Irene and Lee. *Geophys. Res. Lett.,* **40,** 5451–5455, doi:10.1002/2013GL057906.

Simpson, J. H., and R. A. Nunes, 1981: The tidal intrusion front: An estuarine convergence zone. *Estuarine Coastal Shelf Sci.,* **13,** 257–266, doi:10.1016/S0302-3524(81)80024-2.

Simpson, J. E., and P. F. Linden, 1989: Frontogenesis in a fluid with horizontal density gradients. *J. Fluid Mech.,* **202,** 1–16, doi:10.1017/S0022112089001072.

Traykovski, P., W. R. Geyer, and C. Sommerfield, 2004: Rapid sediment deposition and fine-scale strata formation in the Hudson estuary. *J. Geophys. Res.,* **109,** F02004, doi:10.1029/2003JF000096.

Warner, J. C., W. R. Geyer, and J. A. Lerczak, 2005: Numerical modeling of an estuary: A comprehensive skill assessment. *J. Geophys. Res.,* **110,** C05001, doi:10.1029/2004JC002691.

Woodruff, J. D., W. R. Geyer, C. K. Sommerfield, and N. W. Driscoll, 2001: Seasonal variation of sediment deposition in the Hudson River estuary. *Mar. Geol.,* **179,** 105–119, doi:10.1016/S0025-3227(01)00182-7.